Contents lists available at ScienceDirect

Journal of Materials Science & Technology

journal homepage: www.jmst.org

Microstructural evolution of aluminum alloy during friction stir welding under different tool rotation rates and cooling conditions

X.H. Zeng [a,b], P. Xue [a], L.H. Wu [a,*], D.R. Ni [a], B.L. Xiao [a], K.S. Wang [c], Z.Y. Ma [a,*]

[a] *Shenyang National Laboratory for Materials Science, Institute of Metal Research, Chinese Academy of Sciences, Shenyang 110016, China*
[b] *University of Chinese Academy of Sciences, Beijing 100049, China*
[c] *School of Metallurgical Engineering, Xi'an University of Architecture and Technology, Xi'an 710055, China*

ARTICLE INFO

ABSTRACT

The microstructural evolution during friction stir welding (FSW) has long been studied only using one single welding parameter. Conclusions were usually made based on the final microstructure observation and hence were one-sided. In this study, we used the "take-action" technique to freeze the microstructure of an Al-Mg-Si alloy during FSW, and then systematically investigated the microstructures along the material flow path under different tool rotation rates and cooling conditions. A universal characteristic of the microstructural evolution including four stages was identified, i.e. dynamic recovery (DRV), dislocation multiplication, new grain formation and grain growth. However, the dynamic recrystallization (DRX) mechanisms in FSW depended on the welding condition. For the air cooling condition, the DRX mechanisms were related to continuous DRX associated with subgrain rotation and geometric DRX at high and low rotation rates, respectively. Under the water cooling condition, we found a new DRX mechanism associated with the progressive lattice rotation resulting from the pinning of the second-phase particles. Based on the analyses of the influencing factors of grain refinement, it was clearly demonstrated that the delay of DRV and DRX was the efficient method to refine the grains during FSW. Besides, ultra-high strain rate and a short duration at high temperatures were the key factors to produce an ultrafine-grained material.

© 2019 Published by Elsevier Ltd on behalf of The editorial office of Journal of Materials Science & Technology.

1. Introduction

Friction stir welding (FSW) is a relatively new solid-state joining technology that has been widely studied in metals, composites, and even polymer-based materials [1–5]. A large number of studies have shown that FSW is especially suitable for the Al alloys due to its various advantages over conventional fusion welding techniques, such as much finer grains and higher properties of the FSW Al joints. As we know, FSW is involved in both mechanical and thermal processes, which mainly include material flow with the welding tool rotation, and heating and post-welding cooling steps [1]. It is well accepted that the plastic deformation and thermal exposure during FSW induce the occurrence of dynamic recrystallization (DRX) in the stir zone (SZ) [4–6]. Therefore, understanding the microstructural evolution of Al alloys during FSW and the influencing factors is of practical importance for determining the processing window of FSW and the final properties of the joints.

Recently, friction stir processing (FSP), a relatively new severe plastic deformation (SPD) process based on the basic principles of FSW [7], has been proven to be an effective and versatile metal-processing technique for producing fine-grained microstructures [7–9] and surface composites [10]. Like other SPD processes, fine-grained or/and ultrafine-grained (UFG) microstructure is one of the main characteristics of FSP Al alloys [11,12] and the grain evolution behavior is one of the key concerns for FSP Al alloys.

So far, three types of DRX mechanisms have been proposed as the main grain evolution mechanisms of Al alloys during FSW/FSP (hereafter referred to as FSW due to their same process principle). Early investigations suggested that the main grain evolution mechanism was continuous dynamic recrystallization (CDRX), which involves the formation of new grains by the gradual misorientation increase of the subgrains [9,13,14]. Later, based on the experimental observation that the new grains in the SZ were smaller than the original subgrains [15], discontinuous dynamic recrystallization (DDRX), which includes classical nucleation and growth of strain-free grains [16], was considered to be the main grain evolution mechanism during the FSW of Al alloys [16,17]. Lastly, geometric dynamic recrystallization (GDRX) was found to be another DRX
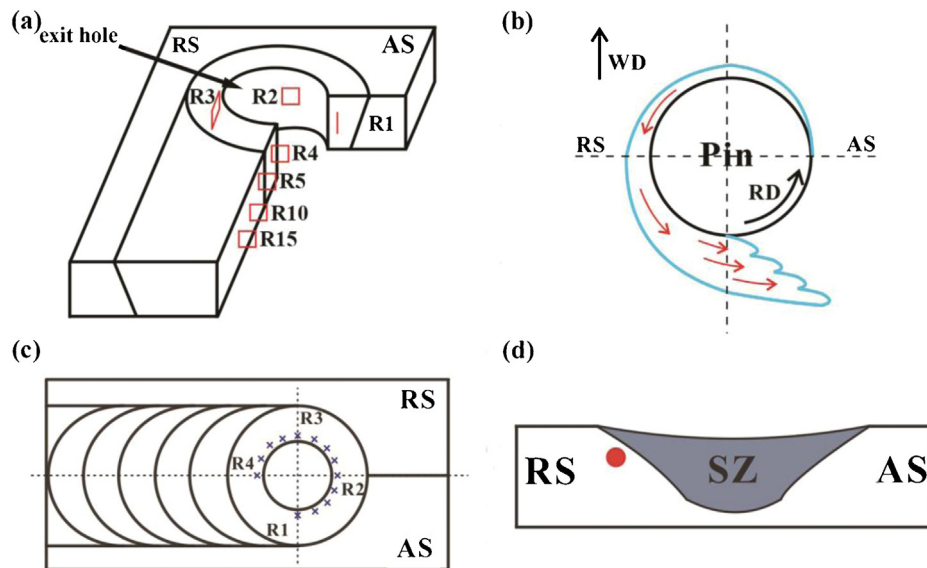

Fig. 1. (a) Sampling schematics for TEM examinations, (b) schematic illustration of material flow around the pin, (c) the placement of vickers hardness tests in the "take-action" samples and (d) the placement of thermocouples shown by the red dot.

mechanism during FSW of Al alloys [16,18]; the main evidence for GDRX was related to a few retained high-aspect ratio fibrous grains [18].

Moreover, the grain evolution mechanisms are believed to greatly depend on welding conditions. For example, CDRX associated with subgrain rotation occurred in the deformed Al alloys at a very high temperature of $0.9T_m$ [19–21]. However, DDRX was usually observed when the deformation temperatures were greater than $0.3T_m$ [16]. Meanwhile, the shapes and sizes of the grains in the SZ of the FSW Al alloys are different at different welding parameters and cooling methods. Wang et al. [12] found that additional water cooling during FSW was an effective strategy to decrease the size of the grains. Zeng et al. [22] reported that the elongated nano-sized grains were observed in the SZ of FSW 6061Al-T6 alloy at a low heat input of 400 rpm and rapid water cooling.

Thus, there has been a consensus that DRX occurs in the FSW of Al alloys with high stacking fault energy and the microstructural evolution mechanisms during FSW vary with welding conditions. However, due to complex strain paths and final structures with the instant deformed or recrystallized characteristics almost disappearing [16], the detailed microstructural evolution during FSW has not been elucidated clearly. Moreover, compared with the other SPD processes, FSW has distinct process characteristics that include rapid transients and steep gradients in temperature, strain, and strain rate [16]. Thus, the microstructural evolution during FSW is quite different from that in other SPD processes.

The grain evolution process during post-welding cooling is also of great significance. A significant grain-coarsening phenomenon, which occurs during the post-welding cooling, has been clearly demonstrated in several studies [23,24]. Mironov et al. [23] suggested that grain growth during the post-welding cooling was most pronounced above $0.7T_m$. Nevertheless, some studies [13] showed that the cooling rate was the key factor influencing the grain growth during post-welding cooling. Due to the instantaneity of FSW [25,26], it was very difficult to observe grain coarsening during the post-welding cooling, and therefore this phenomenon still needs an in-depth investigation.

In this study, the formation and growth of new grains during FSW were investigated using the "take-action" technique of FSW (the rotating tool is suddenly stopped, then withdrawn imme-diately), which can retain the information of transient material deformation around the pin [9,27]. Some grain refinement models are proposed to describe the grain evolution during FSW.

2. Experimental procedure

Commercial 6061Al-T6 sheets (3 mm thick), which contain 1.08 Mg, 0.59Si, 0.21Cu, 0.3 Fe, 0.25Zn, 0.01Cr, and 0.01Ti (wt.%) with a balance of Al, were used in this study. The sheets were subjected to FSW along the rolling direction with a tool tilt angle of 2.8°. The tool used in this study was made of heat-treated tool steel with a 12 mm diameter shoulder and a pin 4 mm in root diameter and 2.5 mm in length (taper threaded pin).

To understand the effect of FSW conditions on the grain evolution during FSW, FSW was conducted at different tool rotation rates of 400 and 1000 rpm for a constant traverse speed of 100 mm·min^{-1}, defined as 400-A and 1000-A for the samples with air cooling, respectively, and as 400-W for the sample with water cooling.

At the end of the FSW joints, the rotating tool was quickly lifted from the workpieces and the material surrounding the exit hole was immediately quenched with water to freeze the microstructures of the different regions around the exit hole (Fig. 1(a)). According to the rule of material flow (Fig. 1(b)) [28,29], the material rotates with the pin and moves from the advancing side (AS) to the trailing side sequentially. Therefore, regions around the exit hole were defined as R1, R2, R3, and R4, respectively. The regions that were 5, 10, and 15 mm away from the center of the exit hole, were defined as R5, R10, and R15, respectively, as illustrated in Fig. 1(a). The observation areas (R1 to R15) were in the mid-thickness of samples. Meanwhile, to avoid the influence of the pullout of the rotating tool at the end of the welding, the distances between R1, R2, R3, R4 and the exit hole were about 0.2 mm.

The microstructures of the FSW samples at the midsections of different regions around and behind the exit hole (Fig. 1(a)) were investigated by transmission electron microscopy (TEM). From a large number of TEM images of the related samples, the statistical distributions of the grain size and average grain size of the related samples can be obtained, by using the linear intercept method. TEM foil specimens were prepared by twin jet electro-polishing using a solution of 30 mL HNO$_3$ and 70 mL CH$_3$OH at a tempera-
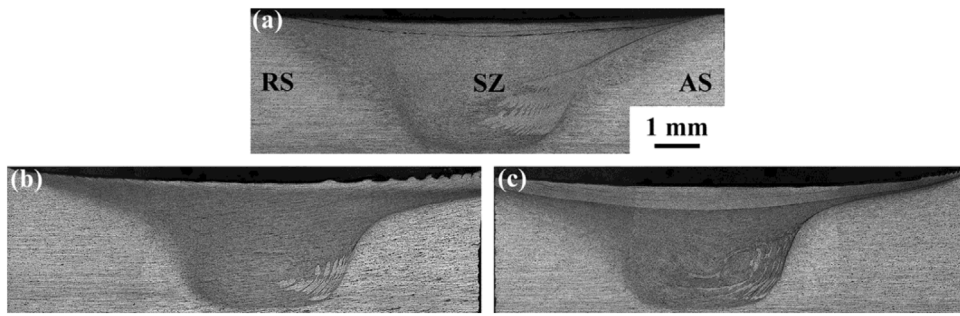
Fig. 2. Macrostructural characteristics of FSW 6061Al-T6: (a) 1000-A, (b) 400-A, and (c) 400-W.
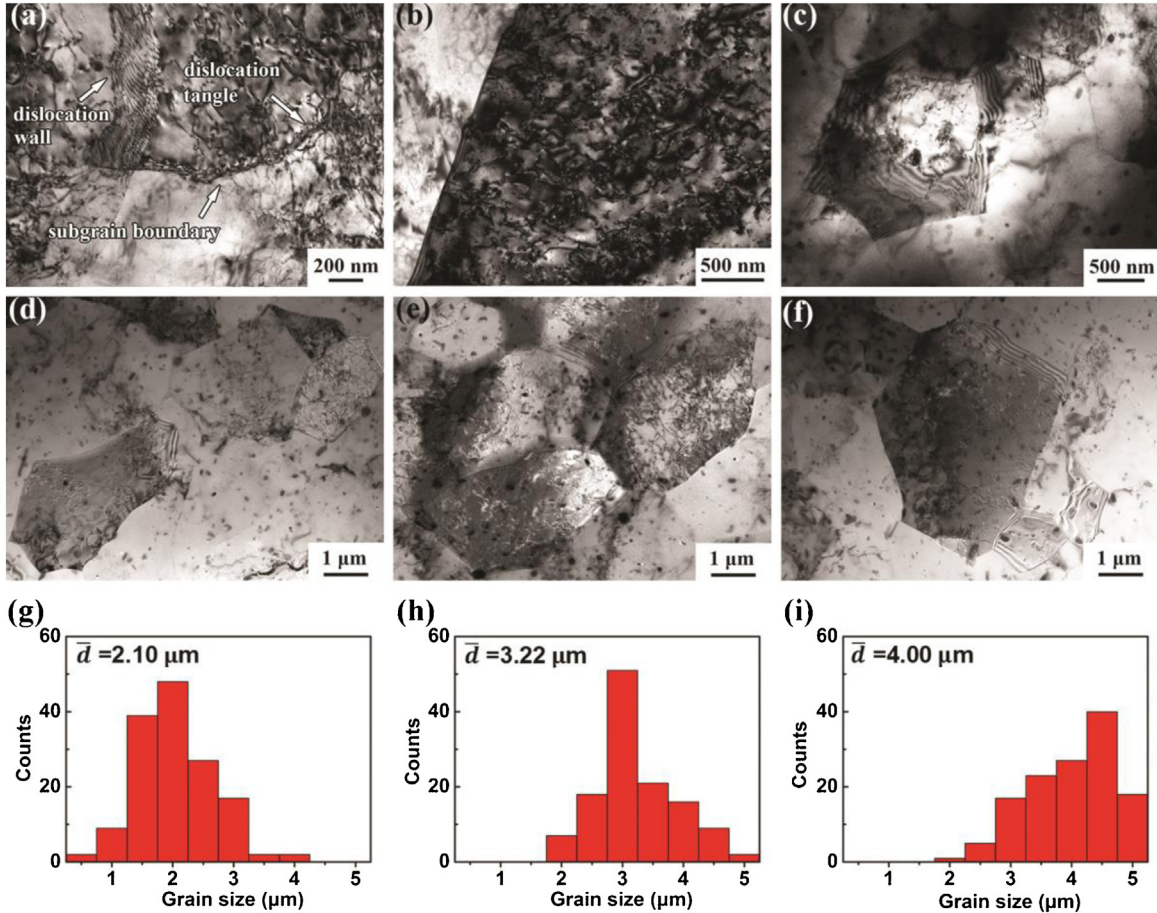

Fig. 3. Typical TEM images showing microstructures in (a) R1, (b) R2, (c) R3, (d) R4, (e) R5 and (f) R15 of 1000-A sample. Statistical distributions of grain size in (g) R4, (h) R5 and (i) R15.

ture of −30 °C and a voltage of 10 V. Electron backscatter diffraction (EBSD) was used to characterize and analyze the microstructures of R1 for the 400-A sample. The specimens for EBSD analysis were prepared by electrolytic polishing at a temperature of −30 °C and a voltage of 12 V with a solution consisting of 10 mL HClO$_4$ and 90 mL CH$_3$CH$_2$OH.

Vickers hardness tests were conducted on the horizontal sections parallel to the welding direction of the samples using a load of 50 g for a holding time of 15 s. The hardness profiles were obtained by measuring the "take-action" samples from R1 to R4 at an equal interval, as shown in Fig. 1(c). The temperature history of the region near the SZ during FSW was monitored and recorded using K-type thermocouples. The placement of the thermocouples is shown in Fig. 1(d).

3. Results

3.1. Microstructural characterization during material flow

Fig. 2 shows the cross-sectional macrostructures of the FSW samples at different tool rotation rates and cooling conditions. It is clear that no defects were detected under the investigated welding parameters. All the FSW samples exhibited basin-shaped SZs with wide top regions. Further, according to the cross-sectional macrostructures of the FSW samples, the mid-thicknesses of the samples were in the probe affected zone (PAZ). Thus, the observation areas (R1 to R15) were in the PAZ.

From the analysis of Fig. 1(a), the material flow path during FSW was from R1 to R15 sequentially. Fig. 3(a)–(f) show the bright-field
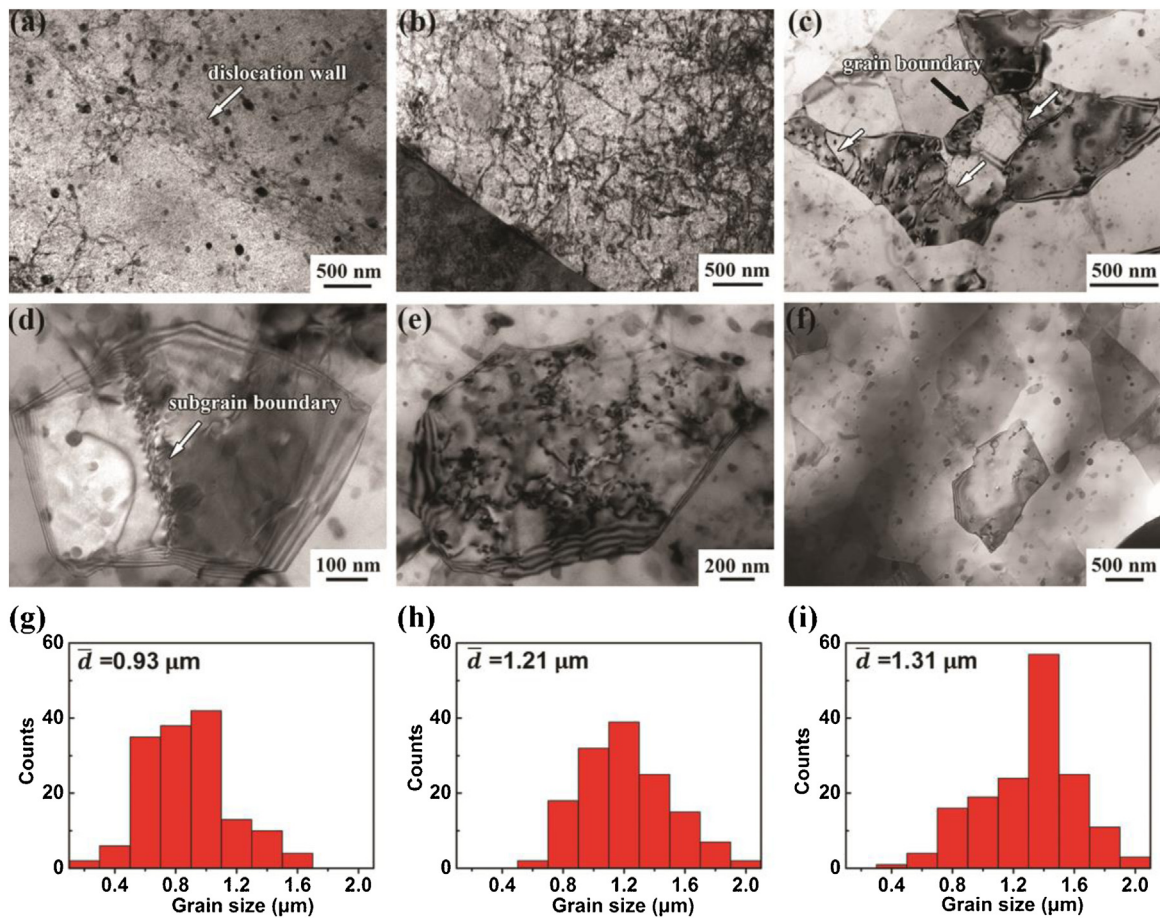
Fig. 4. Typical TEM images showing microstructures in (a) R1, (b) R2, (c) R3, (d) R4, (e) R5 and (f) R15 of 400-A sample. Statistical distributions of grain size in (g) R4, (h) R5 and (i) R15.

TEM images of various regions in the 1000-A sample. In the initial deformation region (R1), a high-density of dislocation tangles and dense dislocation walls were randomly distributed in the original grains (marked by white arrows in Fig. 3(a)). Meanwhile, subgrains with sharp boundaries were observed and their misorientations were large, according to the large contrast between adjacent subgrains. In R2, a mass of dislocations was observed in the original grains (Fig. 3(b)). When the material flowed into R3, new equiaxed grains with an average size of 1.54 μm formed (Fig. 3(c)). In the region behind the pin (R4), slightly elongated grains with some dislocations were obtained (Fig. 3(d)) and the grain size ranged from 0.52 μm to 4.00 μm (with an average of 2.10 μm), as shown in Fig. 3(g). In R5 and R15 (Fig. 3(e) and (f)), the average size of the elongated grains increased to 3.22 μm and 4.00 μm (Fig. 3(h) and (i)), respectively.

Fig. 4(a)–(f) show the bright-field TEM images of various regions in the 400-A sample. In the initial deformation region (R1), dislocation walls were formed in the original grains (Fig. 4(a)). In R2, similar to R2 in the 1000-A sample, a mass of dislocations was observed in the original grains (Fig. 4(b)). When the material flowed into R3, high aspect ratio grains with serrated grain boundaries were observed, and some subgrain boundaries (SGBs, white arrows) were randomly distributed in the deformed grains (Fig. 4(c), the black arrow denotes the high angle boundaries (HAGBs)). In R4, new equiaxed grains with some SGBs and dislocations were formed (Fig. 4(d)), and the average size of these grains was 0.93 μm, as shown in Fig. 4(g). In R5 and R15 (Fig. 4(e) and (f)), the average size of the equiaxed grains increased to 1.21 μm and 1.31 μm (Fig. 4(h) and (i)), respectively.

Compared to the 1000-A and 400-A samples, the microstructures of the 400-W sample were rather different, as shown in Fig. 5(a)–(f). In the initial deformation region (R1), only a mass of dislocations was observed in the original grains (Fig. 5(a)). In R2, SGBs were observed in the original grains and the misorientations were relatively large (Fig. 5(b)), as discerned by the large contrast between adjacent subgrains. The microstructures of R3 (Fig. 5(c)) were similar to those of R1; a mass of dislocations was observed in the original grains. When the material flowed into R4, new equiaxed fine grains with an average size of 0.43 μm (ranging from 0.1 to 0.8 μm, Fig. 5(g)) were formed (Fig. 5(d)). Spherical second-phase particles ($MgSi_2$, white arrows)[30,31] were mostly distributed along the boundaries of the new grains. Meanwhile, the newly formed equiaxed fine grains showed some directional distribution (long black arrow). In R5 and R15 (Fig. 5(e) and (f)), the microstructural characteristics of the new grains and second-phase particles were similar to those in R4. The average size of the grains in R5 and R15 slightly increased to 0.54 and 0.55 μm (Fig. 5(h) and (i)), respectively.

3.2. Microhardness variation during material flow with the tool

Fig. 6 depicts the variation of microhardness with positions from R1 to R4 around the pin for the "take-action" samples at different welding conditions. Three important observations could be made. First, the microhardness profile of the 1000-A sample initially increased and then decreased, while the profiles of the 400-A and 400-W samples exhibited an "increasing, decreasing, increasing" trend. Second, the sudden change in microhardness in the
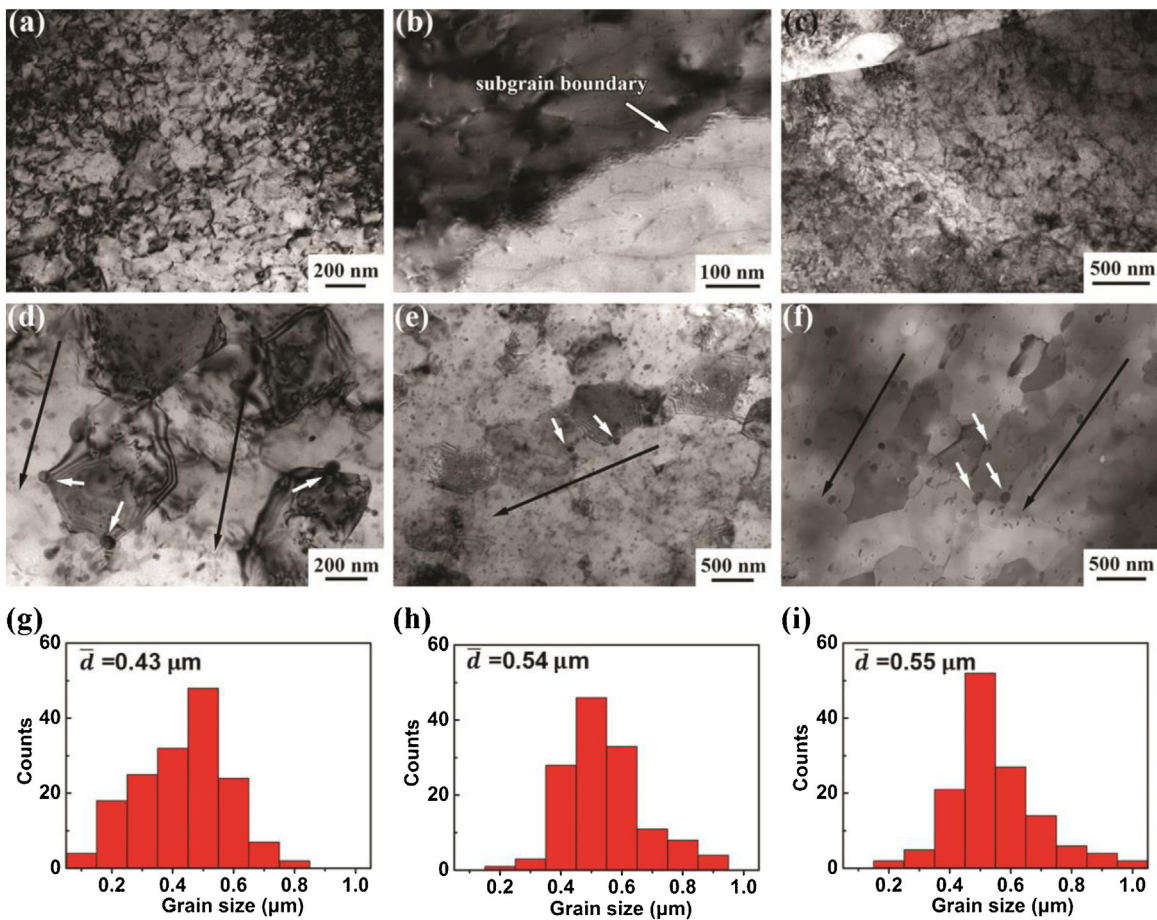
Fig. 5. Typical TEM images showing microstructures in (a) R1, (b) R2, (c) R3, (d) R4, (e) R5 and (f) R15 of 400-W sample. Statistical distributions of grain size in (g) R4, (h) R5 and (i) R15.
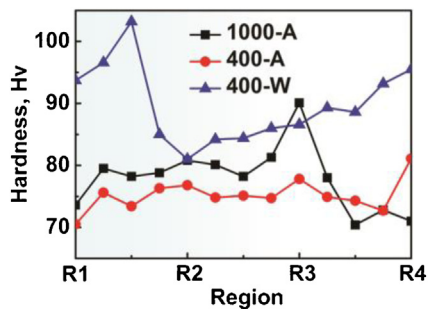

Fig. 6. Microhardness profiles of FSW samples at different welding and cooling conditions.

Fig. 7. Temperature histories of FSW samples under different FSW conditions.

microhardness profiles appeared near R3, R4, and R2 for the 1000-A, 400-A, and 400-W samples, respectively. Third, before R3, the microhardness changing trends for the 1000-A and 400-A samples were the same; the microhardness value of the 1000-A sample was larger than that of the 400-A sample in the same region.

3.3. Temperature history during FSW

Fig. 7 shows the temperature histories of the regions near the SZ at different tool rotation rates and cooling conditions. It is clear that the peak temperature increased with the rotation rate. Meanwhile, the peak temperature for the joint obtained by air cooling was higher than that obtained by water cooling at the same rotation rate. The peak temperature in the region near the SZ was as high
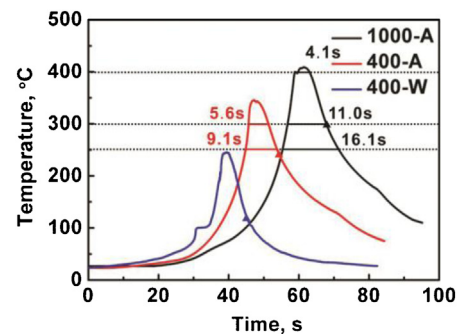
as 410 °C for the 1000-A sample, and was only about 245 °C for the 400-W sample. Thus, decreasing the rotation rate and using water cooling are effective strategies to decrease the peak temperature and duration at high temperatures. However, it should be noted that using water cooling cannot obviously increase the cooling rate. According to Fig. 7, the cooling rates of the 1000-A, 400-A, and 400-W samples during post-welding cooling were similar, i.e. $\bar{1}9.3$ °C·s^{-1}, $\bar{1}8.8$ °C·s^{-1}, and $\bar{2}0.6$ °C·s^{-1}, respectively (calculated from the points of the highest temperature to the marked points on the temperature curves; the marked points corresponded to the temperatures at the positions R10 at different parameters). Besides, the duration time at high temperature for the 1000-A sample was long. For example, the duration time over 400 °C, 300 °C, and 250 °C for the 1000-A sample were 4.1 s, 11.0 s, and 16.1 s, respectively.
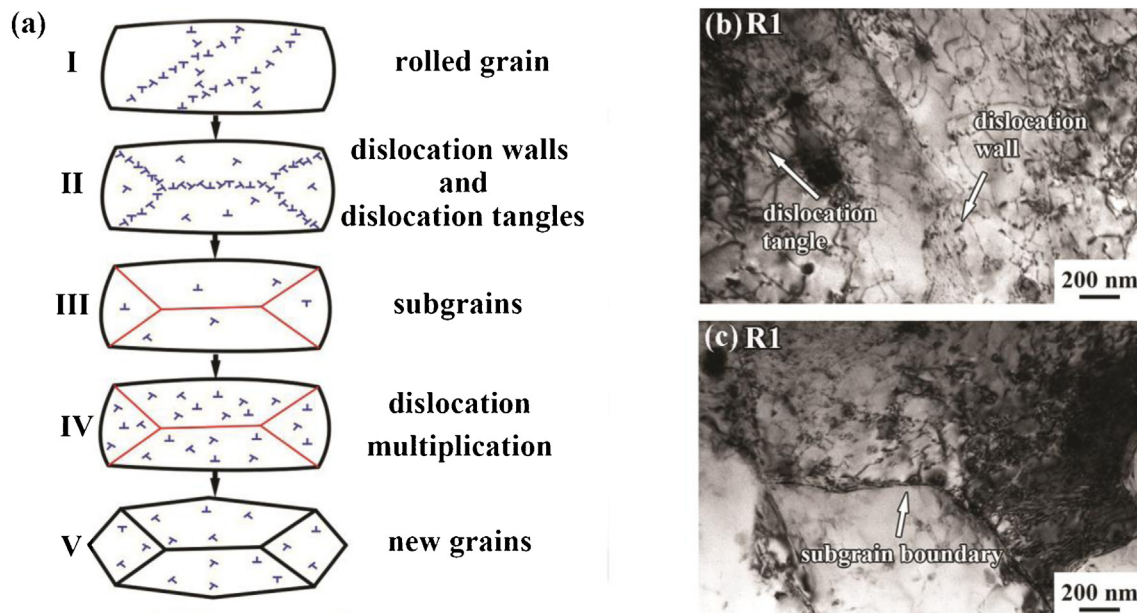
Fig. 8. (a) Schematic illustration of grain evolution in 1000-A sample, (b) and (c) typical microstructures in R1.

On the contrary, there was no duration over 250 °C for the 400-W sample.

4. Discussion

4.1. New grain formation mechanisms during material flow at different FSW parameters

It is well known that original grains were deformed, and then recrystallized to form new grains during material flow [13]. At a high rotation rate of 1000 rpm with air cooling, various dislocation activities (Fig. 3) were normally induced, including dislocation slip, accumulation, interaction, tangling, and spatial rearrangement in order to accommodate the plastic strain generated during FSW. Based on the microstructural features in the 1000-A sample, the mechanism of new grain formation is schematically illustrated in Fig. 8(a).

Owing to plastic deformation and thermal exposure, dislocation activities led to the formation of dislocation tangles and dense dislocation walls in the original grains (Stage II in Fig. 8(a)), as can be clearly seen in R1 (Figs. 3(a) and 8 (b)). At a certain strain level, to minimize the total energy of the system, dislocation tangles and dense dislocation walls transformed into SGBs, and the original grain was separated into individual cells (Stage III in Fig. 8(a)), as can be clearly seen in Fig. 8(c). Stages II and III are typical characteristics of the dynamic recovery (DRV) mechanism [16,32]. Thus, the microhardness of the 1000-A sample in R1 (74 Hv) was lower than that of the parent material (96 Hv).

With a further increase in the strain, dislocation multiplication (DM) occurred in the original grains in R2 (Stage IV in Fig. 8(a)). With gradually increasing deformation, the subgrains rotated and changed into new equiaxed grains in R3 (Stage V in Fig. 8(a)), which is the so-called CDRX. The new grain formation was a result of the gradual increase in the misorientation between the subgrains until HAGBs were formed [33]. Similar grain formation processes were observed in the Al-Cu-Mg alloy during multiple laser shock processing (LSP) [34]. When the material moved from R3 to R4, slightly elongated grains were formed due to further deformation, as shown

in Fig. 3(d). Thus, the formation of new grains at a high rotation rate with air cooling in FSW was associated with dislocation activities and subgrain rotation.

At a lower rotation rate of 400 rpm with air cooling, the mechanism of new grain formation was different (Fig. 9(a)). During deformation, dislocation activities led to the formation of dense dislocation walls, which was a typical characteristic of DRV, as shown in Fig. 4(a). Meanwhile, the original grains became elongated and flattened and the grain boundaries were serrated (Stage I in Fig. 9(a)), as clearly seen in the EBSD map of R1 (Fig. 9(b)). Such high-aspect ratio fibrous grains in "stop-action" samples of 2195Al alloy were also observed by Prangnell et al. [18]. With an increase in the strain, the size of the boundary serrations eventually became comparable to the grain thickness (Fig. 9(c)), as shown in Stages II and III in Fig. 9(a). With a continued increase in the deformation, the serrated grain boundaries interpenetrated each other resulting in a microstructure of small equiaxed grains (Stage IV in Fig. 9(a)), as clearly seen in R4 (Fig. 4(d)). The serrated grain boundaries and the migration of SGBs and HAGBs were the characteristics of new grain formation under these welding conditions, which was the so-called GDRX [16,18,24].

It is known that temperature influences the grain evolution during deformation [31,35,36]; water cooling has proven to be an effective method for reducing the peak temperature during FSW [12,37]. Thus, the mechanism of new grain formation at a low rotation rate of 400 rpm with water cooling was quite different compared to the other conditions in this study, as shown in Fig. 10(a).

Because of the interactions of the deformation substructures, SGBs were formed in the original grains, as shown in Fig. 5(b) (Stage I in Fig. 10(a)). Meanwhile, the microhardness value of the 400-W sample reduced due to DRV in R2. With an increase in the strain, because of the pinning effect of the second-phase particles, HAGB sliding can occur only on parts of the boundaries, whilst other regions had to accommodate the strain by plastic deformation (Stage II in Fig. 10(a)). These effects led to shear and local lattice rotation, as shown in Stage III in Fig. 10(a). This grain formation mechanism led to spherical second-phase particles being mostly
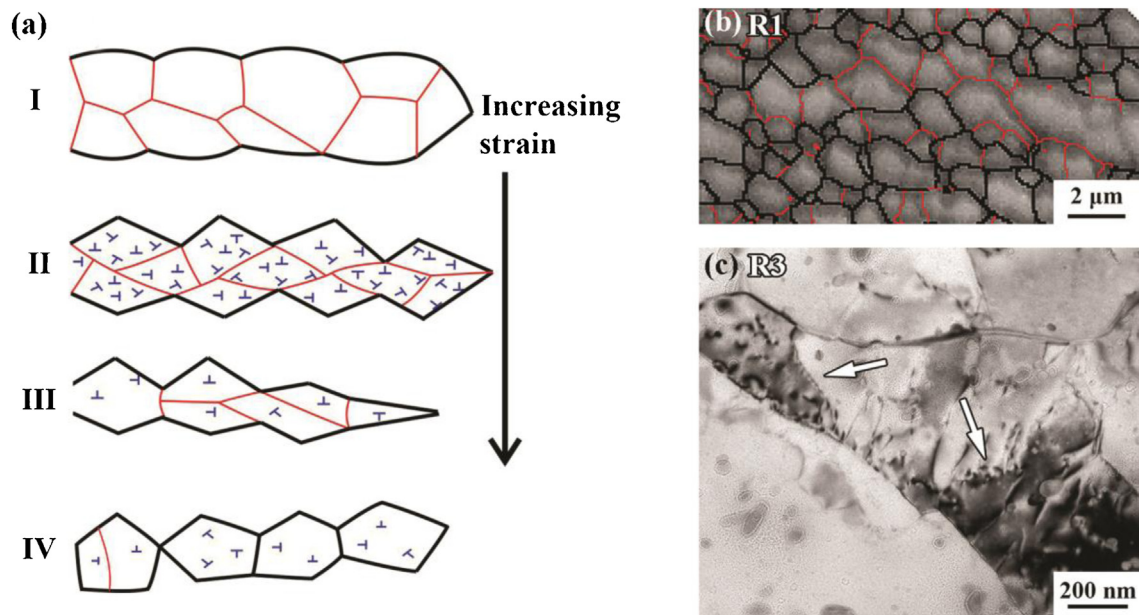
Fig. 9. (a) Schematic illustration of grain evolution in 400-A sample, (b) EBSD map of R1 and (c) typical microstructures in R3.
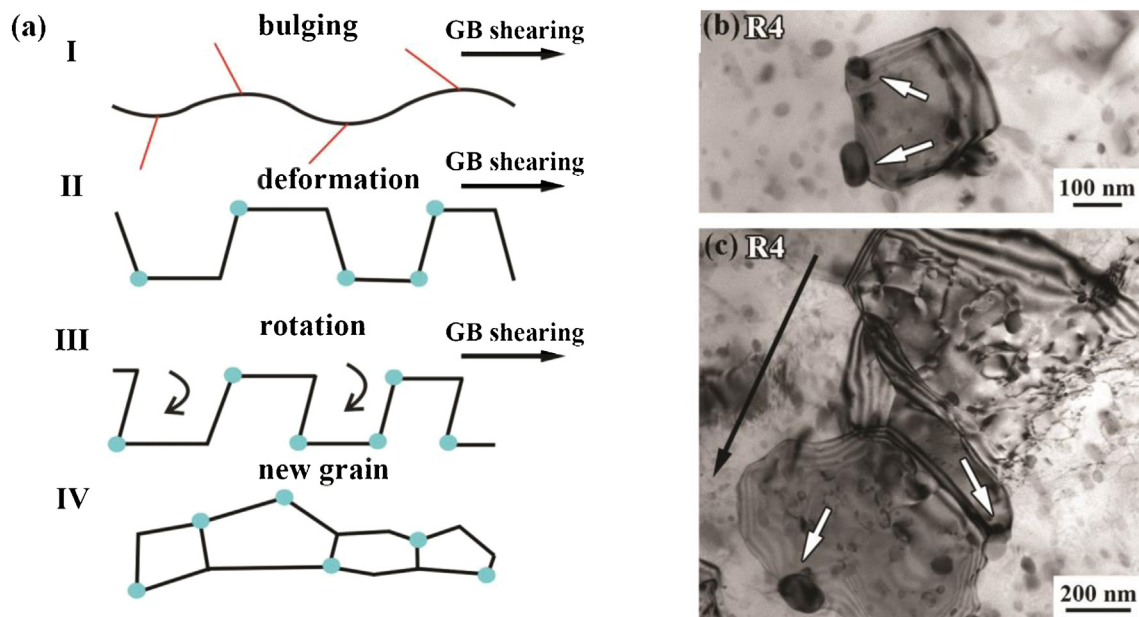

Fig. 10. (a) Schematic illustration of grain evolution in 400-W sample, (b) and (c) typical microstructures in R4.

distributed at the boundaries of the new grains (Fig. 10(b)) and new equiaxed fine grains showed some directional distribution, as can be clearly seen in R4 (Figs. 5(d) and 10 (c)).

Therefore, for the water cooling condition, the DRX mechanism was mainly related to progressive lattice rotation resulting from the pinning of the second-phase particles, which is a kind of rotation recrystallization mechanism. This mechanism, as far as we know, has never been proposed during SPD before. Although a similar rotation recrystallization mechanism was observed during the compression deformation of Al-5Mg alloy [38] and copper [39], it was dependent on boundary sliding and twinning rather than the pinning of second-phase particles. Therefore, this finding in this study enlarged the knowledge of DRX and FSW fields.

4.2. Universal characteristics of microstructural evolution during FSW at different processing parameters

Based on the discussions above, different DRX mechanisms have been identified during FSW of Al alloys with different welding parameters; however, some common characteristics on the microstructural evolution were also observed. Based on the microstructural features in Figs. 3–5 and the schematic illustration of grain evolution in Figs. 8–10, it is suggested that the grain evolution process during material flow at all the welding parameters includes three basic stages: (a) DRV in the original grains, (b) DM in the original grains and (c) formation of new grains, as shown in Fig. 11(a). The differences in the grain evolution mechanisms at different tool rotation rates and cooling conditions were the degree and progress of each stage, as shown in Fig. 11(b).
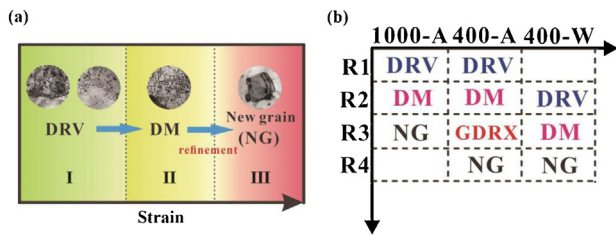
Fig. 11. (a) Progress of grain evolution during FSW, (b) schematic illustration of microstructural characteristics in different regions of 1000-A, 400-A and 400-W samples.

The DRV occurred in R1 for the 1000-A and 400-A samples and in R2 for the 400-W sample. This observation suggests that water cooling can hinder the progress of DRV. Furthermore, according to the microstructural features in R1 of these samples (Figs. 3(a) and 4 (a)), the degree of occurrence of DRV in the 1000-A sample was greater than that in the 400-A sample. This phenomenon implies that a high rotation rate promoted the progress of DRV.

With an increase in the strain, similar to DRV, the development of DM was also delayed by water cooling (Fig. 11(b)). It means that the delay of DRV and DM is an effective method to refine the grains. By comparing the grain sizes under three different FSW parameters, it was found that the delay of DRX led to a more obvious grain refinement effect than the delay of DRV. Besides, as we know, DRV and DRX are the competing mechanisms, and DRX usually does not occur during conventional plastic deformation of Al alloys since DRV consumes the stored energy [21]. During FSW, it is well-known that DRX indeed occurs. However, no study has clearly provided the evidence why DRX could take place during FSW rather than the conventional plastic deformation. In this study, it was clearly shown that the occurrence of DRX was just because after DRV, a large DM occurred, which provided the extra stored energy for DRX during FSW. With a continued increase in the strain, new grains were formed in R3 for the 1000-A sample and R4 for the 400-A and 400-W samples. It is generally known that water cooling reduced the peak temperature [10] and thermal exposure increased with an increase in the rotation rate during FSW [40]. Therefore, it can be inferred that heat is an important factor affecting the progress of grain evolution.

4.3. New grain growth during post-welding cooling

Generally, the post-welding cooling during FSW can be divided into two stages [13]: (a) shoulder cooling (R4 to R5) and (b) free cooling (R5 to R15). The grain sizes, measured in R3 to R15 at different tool rotation rates and cooling conditions using a large number of TEM images, are depicted in Fig. 12(a). We observed that the grain sizes for the 1000-A sample were much larger than those for

the 400-A and 400-W samples in the same regions. More importantly, grain coarsening occurred in the 1000-A sample during both shoulder cooling and free cooling. However, at a low rotation rate of 400 rpm, the grains grew only slightly during the shoulder cooling stage, which occurred independently of the cooling methods. The final grain sizes of the 1000-A, 400-A, and 400-W samples were 4.00 μm, 1.31 μm, and 0.55 μm, respectively. Thus, reducing the rotation rate and using water cooling were effective strategies to decrease the final grain size during FSW.

Although the peak temperature of the region near the SZ was lower than that of the SZ itself, the temperature histories of the two regions were similar [40]. Therefore, the temperature histories of the region near the SZ at different tool rotation rates and cooling conditions can reflect the temperature history tendency of the SZ. Based on the results shown in Fig. 7, it can be deduced that a long duration at high temperatures was the reason for grain coarsening in the 1000-A sample during the post-welding cooling. Although there was the similar cooling rate of the 400-A and 400-W samples, the size of the final grains during the post-welding cooling in the 400-A sample was larger than that in the 400-W sample due to the relatively long duration at high temperatures for the 400-A sample (The duration time over 250 °C for the 400-A sample was 9.1 s, while there was no duration over 250 °C for the 400-W sample since its peak temperature was only about 245 °C). Contrary to some literature [13] that claimed that the cooling rate was the key factor influencing the grain growth during post-welding cooling, this study clearly demonstrated that the key factor was the duration at high temperature rather than the cooling rate.

4.4. The key conditions for producing fine grains

The steady grain size results from a dynamic equilibrium between the defect (vacancy, dislocation, and boundary) generation by plastic deformation and defect removal by dynamic restoration during the SPD processes [41,42]. Thus, the strain, strain rate, and temperature (the physical metallurgical parameters of the plastic deformation) are the key parameters, which determine the steady size of the grains. For example, for high-pressure torsion (HPT), Pippan et al. [43] suggested that the main factors influencing the saturated grain size were the temperature, strain rate, and strain path.

The final grain size as a function of temperature during various SPD processes is shown in Fig. 12(b). It is clear that the grain size increases with increasing temperature [44]. It should be pointed out that the temperature was not constant during FSW. Based on the results in Figs. 7 and 12(a), it can be inferred that long durations at high temperatures were the reason for the formation of large new grains and the coarsening of new grains during FSW.

Apart from temperature, the strain rate was the main factor influencing the final grain size of SPD alloys [45]. Table 1 shows the
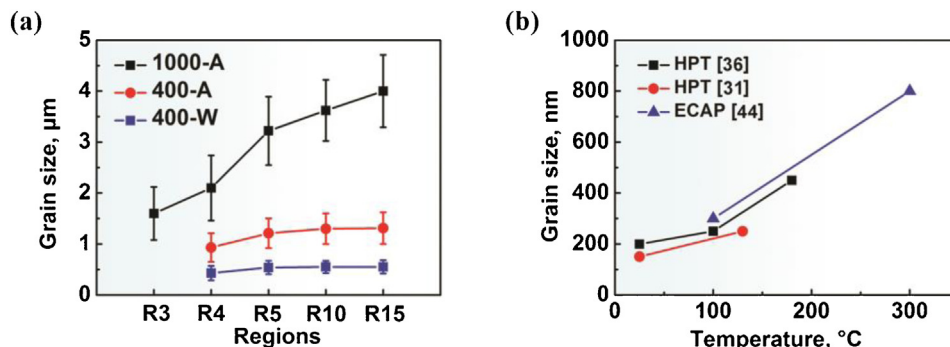

Fig. 12. (a) Grain sizes of FSW samples in different regions, (b) final grain size as a function of temperature during SPD.

Table 1
The effects of strain and strain rate on the minimum grain size and grain shape of SPD Al-Mg-Si alloys or pure Al.

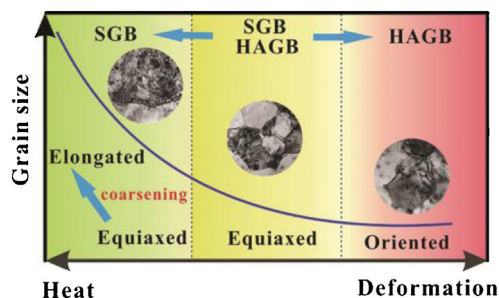| Fabrication method	Strain	Strain rate (s^{-1})	Minimum grain size (nm)	Grain shape	Ref.
ARB	4	<10	300	equiaxed	[46]
ECAP	8	–	200	equiaxed	[45]
HPT	100	<25	100	equiaxed	[36]
FSW	35	75	80	equiaxed/ elongated	[27,28]
SMAT (pure Al)	20-45	$\bar{1}0^3$	30	elongated/lamellar	[47]

Fig. 13. A map of grain evolution modes and grain sizes in FSW Al alloys.

effect of strain and strain rate on the achieved minimum grain size and grain shape in Al-Mg-Si alloys and pure Al with different SPD processes. It is clear that during SPD, the final grain size was largely dependent on the strain rate, rather than the strain. For example, although a maximum strain of 100 was achieved during HPT, the grain size (100 nm) was much larger than that (30 nm) obtained by surface mechanical attrition treatment (SMAT) where the strain was just 20–45 [36,47]. More importantly, nanostructured grains can be obtained by the FSW and SMAT methods due to the ultra-high strain rate [27,28,47]. Moreover, the nanostructured grains in the FSW and SMAT samples consisted of elongated grains or lamellar structures [22,43], which indicated that fine grains retain their original deformed morphology.

Thus, the key conditions for producing fine grains by FSW can be determined to be a short duration at high temperatures and ultra-high strain rate. Zhang et al. [48] investigated the combined effects of strain rate and temperature on the microstructure of Cu using the Zener-Hollomon parameter (Z), which is given by

$$Z = \dot{\varepsilon}\exp(Q/RT) \qquad (4)$$

where $\dot{\varepsilon}$ is the strain rate, R is the universal gas constant and Q is the activation energy for diffusion. With increasing Z, i.e., increasing strain rate and/or decreasing temperature, the UFG microstructure transforms into a mixed nanostructure of nanoscale twin bundles and nanosized grains in Cu processed by dynamic plastic deformation (DPD) [48].

Using the structural information presented above, the grain size, grain evolution mechanisms and microstructure characteristics of the FSW Al alloys can be summarized in Fig. 13. Three regions can be differentiated according to the grain evolution mechanisms and characteristics. At a low Z, deformation during FSW was dominated by dislocation activities and SGB migration. The grains usually exhibited an elongated morphology. New grains grew dramatically during the post-welding cooling and the microstructures were characterized by coarse grains with sizes of 3–5 μm; At a middle Z, SGB and HAGB migration competed with each other during FSW, forming equiaxed grains with sizes of 1–1.5 μm. At a high Z, the grain evolution mechanism was identified as the progressive lattice rotation resulting from the pinning of the second-phase particles, and the characteristics of the microstructures were slightly elongated UFGs with sizes of 400–600 nm. It is apparent from this map that under a large Z condition i.e., water cooling and/or low rota-

tion rate condition is a feasible strategy to obtain finer grains in Al alloys during FSW.

5. Conclusions

In this study, the microstructural evolution mechanism of Al alloys during FSW was investigated using the "take-action" technique of FSW, and the following conclusions can be drawn:

(1) For all welding conditions used, a universal four-stage microstructural evolution along the material flow direction was identified: DRV, dislocation multiplication, new grain formation, and grain growth. The delay of DRV and DRX was the effective way to refine the grains during severe plastic deformation.
(2) The DRX mechanisms in FSW clearly depended on the Z parameter. Under the air cooling condition (a relatively low Z parameter), the grain evolutions were CDRX associated with subgrain rotation and GDRX at high and low rotation rates, respectively. Under the water cooling condition (a large Z parameter), a DRX mechanism of progressive lattice rotation associated with the pinning of the second-phase particles was proposed for the first time.
(3) The key factor controlling the grain size during post-welding cooling was the duration at high temperatures rather than the cooling rate.
(4) An ultra-high strain rate and a short duration at high temperatures were the key factors to produce an ultrafine-grained material in FSW. The final grain morphologies depended on the Z parameter.

Author contributions

X. H. Zeng and P. Xue contributed equally to this work. They conceived the idea and the design of the experiments. X. H. Zeng and L. H. Wu performed the "take-action" technique in the FSW experiments. X. H. Zeng wrote the paper under the supervision of L. H. Wu, D. R. Ni, B. L. Xiao, Z. Y. Ma, and K.S. Wang. All authors participated in the data analysis and discussion.

Acknowledgments

References

[1] G.K. Padhy, C.S. Wu, S. Gao, J. Mater. Sci. Technol. 34 (2018) 1–38.
[2] L.H. Wu, K. Nagatsuka, K. Nakata, J. Mater. Sci. Technol. 34 (2018) 1628–1637.
[3] P. Xue, Z.Y. Huang, B.B. Wang, Y.Z. Tian, W.G. Wang, B.L. Xiao, Z.Y. Ma, Sci. China Mater. 59 (7) (2016) 531–537.
[4] W.F. Xu, Y.X. Luo, W. Zhang, M.W. Fu, J. Mater. Sci. Technol. 34 (2018) 173–184.
[5] L.H. Wu, H. Zhang, X.H. Zeng, P. Xue, B.L. Xiao, Z.Y. Ma, Sci. China Mater. 61 (3) (2018) 417–442.
[6] W.F. Xu, Y.X. Luo, M.W. Fu, Mater. Charact. 138 (2018) 48–55.
[7] A.H. Feng, Z.Y. Ma, Scr. Mater. 56 (2007) 397–400.

[8] C.Y. Liu, B. Qu, P. Xue, Z.Y. Ma, K. Luo, M.Z. Ma, R.P. Liu, J. Mater. Sci. Technol. 34 (2018) 112–118.

[9] J.Q. Su, T.W. Nelson, C.J. Sterling, Mater. Sci. Eng. A 405 (2005) 277–286.

[10] R.S. Mishra, Z.Y. Ma, I. Charit, Mater. Sci. Eng. A 341 (2003) 307–310.

[11] H.J. Zhang, H.J. Liu, L. Yu, Sci. Technol. Weld. Join. 16 (2011) 459–464.

[12] B.B. Wang, F.F. Chen, F. Liu, W.G. Wang, P. Xue, Z.Y. Ma, J. Mater. Sci. Technol. 33 (2017) 1009–1014.

[13] A. Yazdipour, A. Shafiei, M.K. Dehghani, Mater. Sci. Eng. A 527 (2009) 192–197.

[14] K.V. Jata, S.L. Semiatin, Scr. Mater. 43 (2000) 743–749.

[15] C. Rhodes, Scr. Mater. 48 (2003) 1451–1455.

[16] T.R. McNelley, S. Swaminathan, J.Q. Su, Scr. Mater. 58 (2008) 349–354.

[17] X. Sauvage, A. Dédé, A.C. Muñoz, B. Huneau, Mater. Sci. Eng. A 491 (2008) 364–371.

[18] P.B. Prangnell, C.P. Heason, Acta Mater. 53 (2005) 3179–3192.

[19] H.M. Chan, F.J. Humphreys, Acta Metall. 32 (1984) 235–243.

[20] S. Chen, X. Jiang, Mater. Sci. Eng. A 612 (2014) 267–277.

[21] F.J. Humphreys, M. Hatherly, Recrystallization and Related Annealing Phenomena, Elsevier, Oxford, 2004, pp. 415–467.

[22] X.H. Zeng, P. Xue, D. Wang, D.R. Ni, B.L. Xiao, Z.Y. Ma, Sci. Technol. Weld. Joining 23 (6) (2018) 478–486.

[23] D. Yi, S. Mironov, Y.S. Sato, H. Kokawa, Philos. Mag. Abingdon (Abingdon) 96 (2016) 1965–1977.

[24] X.C. Liu, Y.F. Sun, H. Fujii, Mater. Des. 129 (2017) 151–163.

[25] P. Heurtier, M.J. Jones, C. Desrayaud, J.H. Driver, F. Montheillet, D. Allehaux, J. Mater. Process. Tech. 171 (2006) 348–357.

[26] J. Han, J. Chen, L. Peng, S. Tan, Y. Wu, F. Zheng, H. Yi, Mater. Des. 130 (2017) 90–102.

[27] X.C. Liu, C.S. Wu, G.K. Padhy, Scr. Mater. 102 (2015) 95–98.

[28] S. Xu, X.M. Deng, Acta Mater. 56 (2008) 1326–1341.

[29] X.H. Zeng, P. Xue, D. Wang, D.R. Ni, B.L. xiao, Z.Y. Ma, Metall. Mater. Trans. A 49 (2018) 2673–2683.

[30] W.J. Kim, J.Y. Wang, Mater. Sci. Eng. A 464 (2007) 23–27.

[31] G. Sha, K. Tugcu, X.Z. Liao, P.W. Trimby, M.Y. Murashkin, R.Z. Valiev, S.P. Ringer, Acta Mater. 63 (2014) 169–179.

[32] F.J. Humphreys, P.B. Prangnell, J.R. Bowen, A. Gholinia, C. Harris, Philos. Trans. Math. Phys. Eng. Sci. 357 (1999) 1663–1681.

[33] M. Wen, G. Liu, Jf. Gu, W.M. Guan, J. Lu, Appl. Surf. Sci. 255 (2009) 6097–6102.

[34] J.Z. Lu, K.Y. Luo, Y.K. Zhang, C.Y. Cui, G.F. Sun, J.Z. Zhou, L. Zhang, J. You, K.M. Chen, J.W. Zhong, Acta Mater. 58 (2010) 3984–3994.

[35] B. Derby, Acta Metall. Mater. 39 (1991) 955–962.

[36] X. Sauvage, E.V. Bobruk, M.Y. Murashkin, Y. Nasedkina, N.A. Enikeev, R.Z. Valiev, Acta Mater. 98 (2015) 355–366.

[37] P. Xue, B.L. Xiao, Q. Zhang, Z.Y. Ma, Scr. Mater. 64 (2011) 1051–1054.

[38] M.R. Drury, F.J. Humphreys, Acta Metall. 34 (1986) 2259–2271.

[39] A.M. Wusatowska-Sarnek, H. Miura, T. Sakai, Mater. Sci. Eng. A 323 (2002) 177–186.

[40] X.X. Zhang, B.L. Xiao, Z.Y. Ma, Metall. Mater. Trans. A 42 (2011) 3229–3239.

[41] X.C. Liu, H.W. Zhang, K. Lu, Acta Mater. 96 (2015) 24–36.

[42] A.M. Mavlyutov, A.S. Bondarenko, M.Y. Murashkin, E.V. Boltynjuk, R.Z. Valiev, T.S. Orlova, J. Alloys. Compd. 698 (2017) 539–546.

[43] R. Pippan, F. Wetscher, M. Hafok, A. Vorhauer, I. Sabirov, Adv. Eng. Mater. 8 (2006) 1046–1056.

[44] S.Y. Chang, K.S. Lee, S.H. Choi, D. Hyuk Shin, J. Alloys. Compd. 354 (2003) 216–220.

[45] N.V. Thuong, H. Zuhailawati, A.A. Seman, T.D. Huy, B.K. Dhindaw, Mater. Des. 67 (2015) 448–456.

[46] M.R. Rezaei, M.R. Toroghinejad, F. Ashrafizadeh, J. Mater. Process. Tech. 211 (2011) 1184–1190.

[47] X.C. Liu, H.W. Zhang, K. Lu, Science 342 (2013) 337–340.

[48] Y. Zhang, N.R. Tao, K. Lu, Acta Mater. 59 (2011) 6048–6058.